Materials Characterization 193 (2022) 112301

Contents lists available at ScienceDirect

Materials Characterization

journal homepage: www.elsevier.com/locate/matchar

Morphological evolution in nanostructured secondary phases in entropy stabilized oxides

Alexander D. Dupuy *, Julie M. Schoenung

Department of Materials Science and Engineering, University of California, Irvine, Irvine, CA 92697, USA

ARTICLE INFO

Keywords:
High entropy oxides (HEO)
Phase transformation
FIB tomography
Morphological evolution
Nanostructured features
Heat treatment

ABSTRACT

High entropy oxides (HEO), containing equimolar ratios of five or more oxide components, have emerged recently as an important class of materials with a variety of interesting properties. Some, but not all, HEO systems can be classified as entropy stabilized oxide (ESO) materials, which means they have a phase state that is stabilized by entropy. In these materials, the competition between the metastable entropy stabilized and equilibrium enthalpy stabilized phase states leads to a reversible entropic phase transformation and the formation of secondary phases after heat treatment. The morphologies of the secondary phases (i.e., Cu-rich tenorite and Co-rich spinel) in bulk (Co,Cu,Mg,Ni,Zn)O were visualized in three dimensions for the first time by using focused ion beam (FIB) tomography. The Cu-rich tenorite secondary phase is observed to manifest as several highly complex particle morphologies with features in the nanometric regime. These morphologies are influenced by heat treatment conditions and the interaction with the Co-rich spinel secondary phase. Additionally, the morphology is dependent on the size of the secondary phase particles themselves, with the morphology evolving from spheres, to needles, to plates as the particles get larger. These results indicate that several strategies can be implemented to manipulate the morphologies of the secondary phases, making it possible to engineer bulk ESO materials with specific microstructural features. The ability to form complex nanostructured architectures will provide a powerful strategy for controlling behavior and expanding the possible applications of ESO materials.

1. Introduction

The discovery of single-phase rocksalt (Co,Cu,Mg,Ni,Zn)O opened the door for a new class of materials with unique behavior and near boundless potential [1]. These materials, commonly called high entropy oxides (HEO), typically contain five or more oxide components in equimolar amounts and form stable single-phase randomized solid solution structures after processing. They have garnered significant interest since their discovery due to their ability to greatly expand the oxide ceramic compositional space and because of their exceptional properties and stability. HEO materials already show promise as capacitors [2], battery cathodes [3], electrolytes [4], and catalysts [5]. Since the discovery of (Co,Cu,Mg,Ni,Zn)O in 2015, HEO materials have expanded to include new oxide crystal structures such as perovskites [6] and fluorites [7]. Additionally, the high entropy design principle has been applied to other ceramic systems such as borides [8], silicides [9], and carbides [10].

It has been hypothesized that the emergence of a single-phase state in these compositionally complex HEO materials is due to an entropy stabilization effect. However, there is still debate about the role of entropy in HEO materials, as the presence of a high configuration entropy in an oxide system does not necessarily mean that the observed crystal structure is stabilized by entropy. For a material to truly be an entropy stabilized oxide (ESO) it would need to have a metastable entropy-driven single-phase state that outcompetes the free energy of an equilibrium enthalpy-driven multi-phase state. The competition between entropy and enthalpy in ESO materials leads to a reversible entropic phase transformation, which gives rise to a continuum of phase heterogeneity that can be controlled through heat treatment within a specific temperature window. We refer to this range of phase heterogeneity, and the corresponding temperature window, as the “phase spectrum” [11]. For transition metal oxide (Co,Cu,Mg,Ni,Zn)O (referred to here as TM-ESO), the entropy-driven state consists of a single-phase rocksalt randomized solid solution structure that is stable at temperatures above the entropic transformation temperature (~850 °C) and can be retained at room temperature through quenching [12]. The enthalpy-driven state forms when TM-ESO is heat treated within the phase transformation temperature window (650–850 °C), and consists of the rocksalt solid

* Corresponding author.
E-mail address: dupuya@uci.edu (A.D. Dupuy).

https://doi.org/10.1016/j.matchar.2022.112301
Received 24 November 2021; Accepted 10 September 2022
Available online 15 September 2022

solution structure as well as a Cu-rich tenorite secondary phase [11]. Heat treating within the transformation temperature window also results in a complex evolution in cation coordination and oxidation state [13].

In our previous work, we observed that the Cu-rich tenorite secondary phase in coarse grained TM-ESO exhibits several types of morphologies [11]. Scanning electron microscopy (SEM) and energy dispersive X-ray spectroscopy (EDS) analysis revealed that the Cu-rich tenorite secondary phase manifests as sphere- and needle-like morphologies with nanostructured dimensions. The Cu-rich secondary phase emerges both in the grain interior and in the grain boundary. Additionally a Co-rich spinel secondary phase was observed to form in TM-ESO after heat treating at 700 °C [13]. The Co-rich particles adopt a spherical morphology. However, these previous microscopy experiments were performed on polished surfaces using only standard SEM-EDS techniques, displaying 2D cross sections of 3D secondary phase morphologies. As a result, the true morphology of the secondary phases is currently unknown. Further, how heat treatment influences the size and morphology of the secondary phase is still not fully understood.

Focused ion beam (FIB) tomography has emerged as a powerful technique for visually reconstructing and observing the 3D microstructural features of a wide variety of materials [14]. FIB tomography can provide valuable information on the 3D morphology of features such as porosity or secondary phases, leading to insights into gas flow in porous media [15] or conduction networks in solid oxide fuel cells [16]. In FIB tomography, trenches are cut to expose a cuboid of material that contains a region of interest. This cuboid is then serially sectioned by milling one side of the cuboid one "slice" at a time. Individual slices are imaged before milling using the integrated SEM, which is repeated until the cube has been completely milled away. Individual image slices are then combined into a 3D reconstruction for further analysis. A more complete description of FIB tomography, as well as effective techniques for improving the FIB tomography process, can be found in the detailed work of Taillon et al. [17].

The reversible phase transformation and controllable phase heterogeneity in ESO materials provides an opportunity for precise microstructural engineering and control of functional and mechanical behavior. Currently, however, the majority of work in the literature focuses on finding HEO materials that yield a single-phase state. So far only TM-ESO, a perovskite ESO [18], and a fluorite ESO [19] have been shown to convincingly demonstrate a reversible transformation. Additionally, the true morphology of the secondary phases, where they emerge, and how they interact with each other is not well understood. Knowledge of how to control the secondary phase behavior will be critical for controlling the properties of ESO materials and discovering new functionalities.

As discussed above, high entropy stability and the entropic phase transformation is not limited to just one composition or potential application [20]. Therefore, understanding how to control the microstructure of ESO materials will have important implications in a diverse range of materials communities. In this work, we use FIB tomography to explore the 3D morphology of the enthalpy-driven secondary phases in bulk TM-ESO. We find that these nanostructured secondary phases are far more complex than initially thought, prompting a re-evaluation of the understanding of their morphology. Combining FIB tomography and conventional 2D microscopy, we observe that the secondary phases are influenced by heat treatment condition and the presence of other secondary phases. Further, we find that one of the secondary phases exhibits a size dependent morphological evolution. Finally, we provide examples of how our findings might be leveraged to further engineer the microstructure in ESO materials.

2. Experimental methods

TM-ESO nanopowders were prepared using solid state synthesis. CuO (25–55 nm reported particle size, 99.95 wt% purity), MgO (50 nm, 99.95%), NiO (18 nm, 99.98%), ZnO (18 nm, 99.95%), and CoO (50 nm, 99.7%) nanopowders were sourced from US Research Nanomaterials Inc. (Houston, TX, USA). These nanopowders were blended in equimolar amounts using an agate mortar and pestle. A Premium 7 (Fritsch GmbH, Idar-oberstein, Germany) planetary ball mill (PBM) was used to further mill and refine the nanopowders. Milling was performed at 300 rpm for 3 h using silicon nitride jars and milling media and with the nanopowders suspended in isopropanol. This mixture of unreacted nanopowders was then pressed and consolidated using conventional sintering in a 1210BL elevator furnace (CM Furnaces, Bloomfield, NJ, USA) at 1100 °C for 12 h in order to produce bulk samples. The consolidated bulk samples had cylindrical geometries with a diameter of 9.5 mm and a thickness of ~1 mm. Consolidated samples were polished metallographically down to 1 μm diamond spray. Archimedes method was used to measure the density of the as-consolidated samples. All bulk samples in this study exhibit relative densities ≥98% based on a theoretical density of 6.137 g/cm^3 [21].

Guided by our previous work, heat treatment conditions were selected to induce meaningful secondary phase formation [11]. Densified samples were heat treated using the elevator furnace, with quenching being performed by lowering the sample and elevator into the path of a fan blowing room temperature air. The sintered samples were heat treated at 700 °C for 2 h and 12 h, and are referred to here as the 2 h and 12 h samples, respectively. The phase state of the as-consolidated and heat treated samples was assessed using an Ultima III (Rigaku, Tokyo, Japan) X-ray diffraction (XRD) instrument. Quantitative phase analysis was performed using the MAUD Rietveld refinement software [22]. Microstructural analysis was performed using a Regulus 8230 SEM (Hitachi, Tokyo, Japan). Grain size was determined by examining fracture surfaces using SEM. Elemental maps were collected on polished specimen surfaces using a QUANTAX FlatQUAD (Bruker, Billerica, MA, USA) EDS instrument at 3 kV accelerating voltage. Our previous work showed that high spatial resolution elemental maps could be obtained using EDS at low accelerating voltages (3 kV) [11].

FIB tomography was performed using a GAIA3 (Tescan, Brno, Czech Republic) dual beam SEM/FIB system. The tomography process was automated using the Tescan 3D Acquisition Wizard software package. An outline of the FIB tomography process, demonstrated on the 2 h heat treated sample, is illustrated in Fig. 1. Our FIB tomography experiments are performed on the polished surfaces of bulk TM-ESO samples, which have a diameter of 9.5 mm and a thickness of ~1 mm. Then the FIB was used to mill out a cuboid for use during the tomography experiment. A thin protective layer of platinum was first deposited over the region of interest. Tomography experiments were performed on milled rectangular cuboids containing the region of interest and having dimensions of 3 μm × 1 μm × 1 μm. A secondary electron detector was used for imaging the individual slices. This cuboid is serially sectioned using FIB, and micrographs are collected of each individual slice. These slices are analyzed to identify the secondary phases and then used together to build a reconstruction of those secondary phases in 3D.

An example of a FIBed cuboid used for tomography can be seen in Fig. 2a. The example cuboid was prepared from a 12 h sample. Surface layers of the cuboid were etched away using the FIB in order to create slices of the sample that could then be used for reconstructing the cuboid in 3D. Three example slices, corresponding to the front of the cuboid, approximately halfway through the cuboid, and the back of the cuboid, can also be seen in Fig. 2a. In this work, the light and dark regions in the individual slices are interpreted as the secondary phases; the medium gray regions are the primary phase: rocksalt TM-ESO. Under certain conditions FIB etching can influence the observed behavior in some materials due to Ga ion implantation and heat generation [23]. However, our individual slices display consistent features throughout the cuboid as the tomography experiments are being performed, indicating that the FIB etching process and the tomography experiment itself do not influence the behavior of the TM-ESO samples or the morphology of the

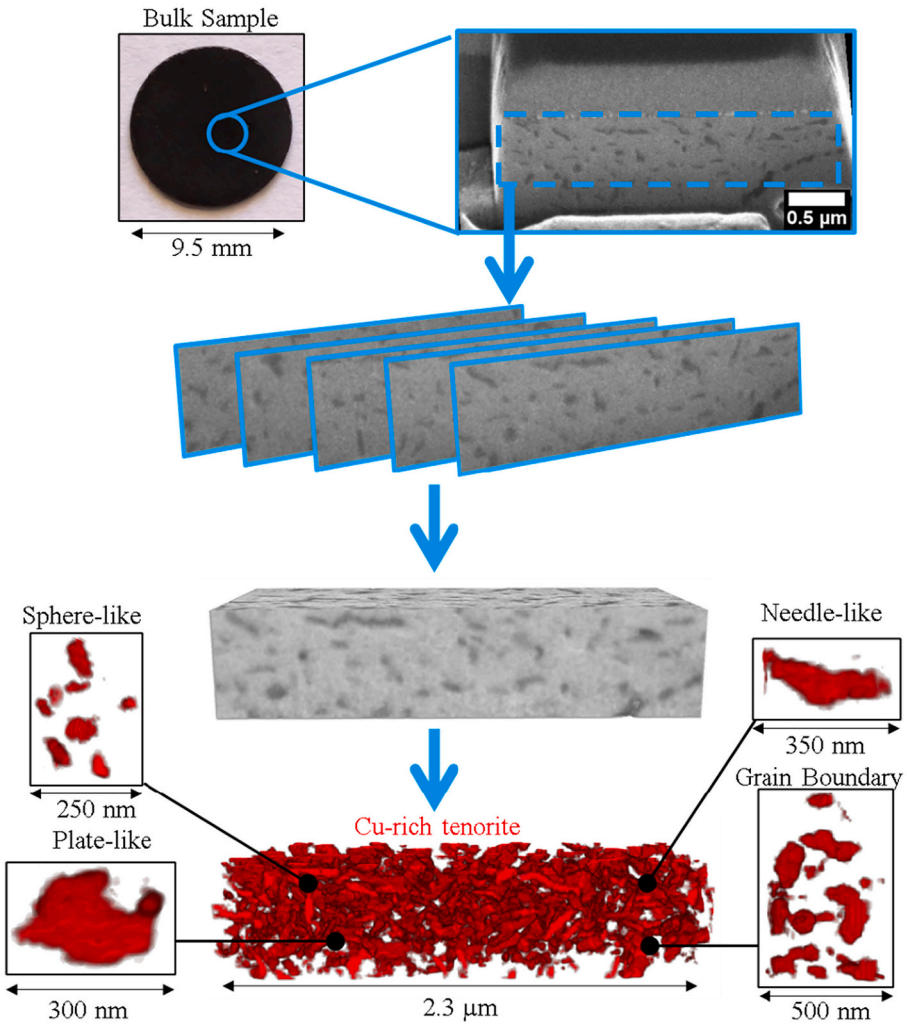

Fig. 1. Synopsis of the FIB tomography process for bulk TM-ESO. An outline summarizing how the 3D reconstruction of the Cu-rich tenorite secondary phase particles is acquired. Here the FIB tomography process is performed on a bulk TM-ESO sample that has been heat treated at 700 °C for 2 h. A bulk cylindrical sample with a diameter of 9.5 mm and a thickness of ~1 mm is used for the analysis. First, a 3 μm × 1 μm × 1 μm cuboid is milled and then serially sectioned and imaged to create "slices". The individually imaged slices are combined and used to reconstruct the cuboid. Image processing is used to isolate and reconstruct the Cu-rich tenorite secondary phase particles, allowing for the individual secondary phase particles to be analyzed. Individual particles representing different particle morphologies or regions of interest are displayed around the reconstruction.

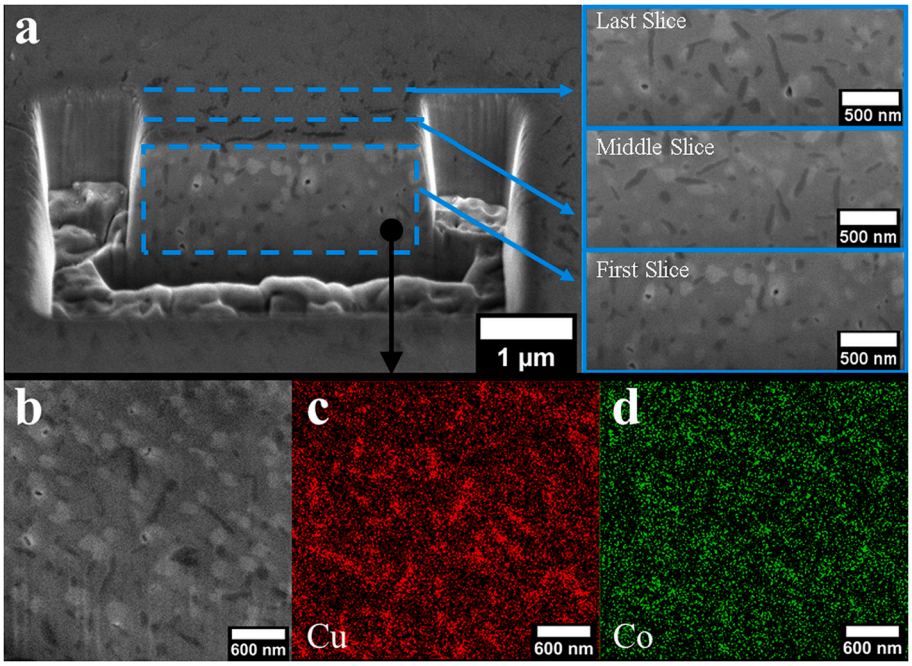

Fig. 2. Example of a bulk TM-ESO milled cuboid. (a) A 3 μm × 1 μm × 1 μm cuboid milled from a bulk TM-ESO sample that has been heat treated at 700 °C for 12 h. The cuboid is ready for the FIB tomography process. The inside of the cuboid is exposed through serial sectioning using FIB, with the blue dashed outline representing the region of interest that is imaged using the SEM. The first, middle, and last image "slice" of the cuboid are displayed, demonstrating that the microstructure can be analyzed through the depth of the cuboid using FIB tomography. (b) A SEM micrograph and corresponding EDS maps for (c) Cu and (d) Co from a representative slice from the cuboid. The dark phase and light phase in the micrograph correspond to the Cu-rich tenorite and Co-rich spinel secondary phases, respectively. The medium gray phase is the primary rocksalt phase. (For interpretation of the references to color in this figure legend, the reader is referred to the web version of this article).

secondary phases.

All image correction, reconstruction, and analysis was performed using ImageJ/FIJI [24]. Intensity gradients within the individual slices were corrected using the trench shading normalization method, as outlined by Taillon et al. [17]. To facilitate quantification, the secondary phase reconstructions were analyzed as individual "particles", whose geometry and dimensions could be measured though image analysis. The secondary phase particles were isolated using the "Segment Phases 3D" tool in the FIJI Xlib package [25]. Quantitative analysis was performed on the morphological features of the secondary phase particles using the FIJI BoneJ package [26]. Four different measurements are used to describe the dimensions of the secondary phase particles: Feret diameter (sometimes called caliper length), thickness, volume, and surface area. Feret diameter is calculated by finding the longest distance between any two points on the particle, while thickness is calculated by finding the largest inscribed sphere that will fit within the particle. Note that particles with a dimension <24 nm were excluded from analysis, as they could not be confidently distinguished from noise or charging effects in the microscope. Particle volume and surface area are measured from a surface mesh constructed from the particles surface voxels. The morphology of the secondary phase particles was quantified using sphericity [27], which is defined as:

$$\Psi = \frac{\pi^{\frac{1}{3}}(6V)^{\frac{2}{3}}}{SA} \quad (1)$$

where V is the volume of the particle and SA is the surface area. Sphericity describes how spherical an object is. $\Psi = 1$ corresponds to a perfect sphere, and $\Psi = 0$ corresponds to an infinite plate [28].

As will be seen below, the morphologies of the secondary phase particles are highly complex, and do not closely match with any particular 3D shape. However, the particles are generally rounded and have a distinct long, middle, and short axis. As such, in this work we have chosen to describe the secondary phase particles as ellipsoids, as this is the shape the particles most closely resemble. Describing the secondary phase particles as ellipsoids allows them to be quantified by three dimensions (Fig. 3). In this work, the longest dimension is denoted as the major diameter, L_{maj}, while the shortest dimension is defined as the minor diameter, L_{min}. The intermediate diameter, L_{int}, is calculated using the other two dimensions from the equation for the volume of an ellipsoid:

$$V = \frac{\pi}{6} L_{maj} L_{int} L_{min} \quad (2)$$

Using the three dimensions to described each secondary phase particle allows for the morphology of the particle to be described using the Zingg and Tucker scheme [27,29,30]. The elongation (= L_{int} / L_{maj}) and the flatness (= L_{min} / L_{int}) were calculated for each secondary phase particle and used to classify the approximate shape of the particle. According to the Zingg and Tucker scheme, particles with an elongation and flatness >0.66 are classified as *equant* (spherical). Conversely, particles with an elongation and flatness <0.66 are classified as *bladed* and resemble plates with all three dimensions being unequal ($L_{maj} \neq L_{int} \neq L_{min}$). Particles which have an elongation >0.66 and a flatness <0.66 are referred to as *tabular* and resemble discs. Finally, particles with an elongation <0.66 and a flatness >0.66 are referred to as *prolate* and resemble needles. A summary of these criteria can be found in Table 1.

In this work, the individual particle volumes are used to describe the overall size of the secondary phase particles. Individual particle dimensions (L_{max}, L_{int}, and L_{min}) are used to convey information about the morphology of the individual secondary phase particles. Throughout this work, the size and morphology of the particles are described relative to the total volume taken up by the secondary phase of interest, which is calculated by summing the individual sizes of all the particles. It is important to note that these comparisons to a "volume" in this work refer to the *volume taken up by the secondary phase*, and not the overall volume of the 3D reconstruction.

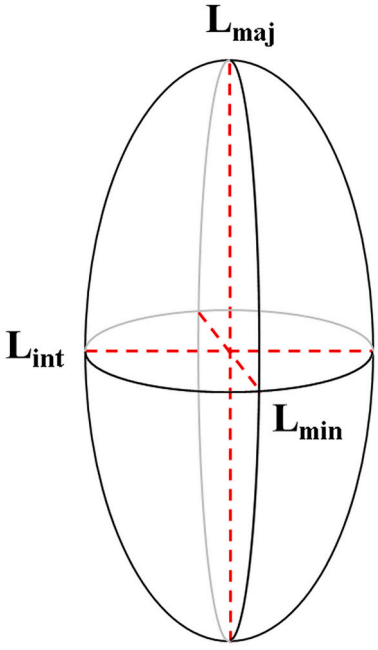

Fig. 3. Schematic illustrating an ellipsoid with relevant dimensions labeled. In this work, all secondary phase particles are modeled as ellipsoids so that they can be described by three dimensions: minor diameter L_{min}, intermediate diameter L_{int}, and major diameter L_{maj}.

3. Results and discussion

3.1. Microstructure and phase state

Using conventional sintering we were able to consolidate TM-ESO nanopowders into fully dense bulk samples. A representative fracture surface microstructure can be observed in Fig. 4a. Conventional sintering at 1100 °C for 12 h yielded as-sintered samples with an average grain size of 25 μm. Such large grain sizes are obtained due to the high temperatures and long hold times used to consolidate the sample. XRD was used to verify the presence of the rocksalt crystal structure in the as-sintered samples (Fig. 4b), which is consistent with what is observed in our previous work [11]. The samples have no signs of any extraneous peaks, indicating that these samples have a single-phase rocksalt structure. EDS analysis was used to verify the phase homogeneity in the as-sintered TM-ESO samples. The as-sintered sample displays no obvious signs of secondary phases (Fig. 4c) or Cu- or Co-rich regions (Fig. 4d and e, respectively). Our previous work found that TM-ESO samples processed under similar conditions exhibit chemical homogeneity down to the nanoscale [12].

The above-mentioned single-phase bulk samples were subsequently

Table 1
Dimensional criteria for assigning a morphological description to each secondary phase particle in the bulk TM-ESO heat-treated samples. The criteria are based on the calculated elongation (= L_{int} / L_{maj}) and flatness (= L_{min} / L_{int}) used in a Zingg and Tucker scheme. The relevance of the specific morphologies to the Cu-rich tenorite and Co-rich spinel secondary phase particles are also listed.

	Flatness	Elongation	Particle type
Sphere	$L_{min} > 0.66L_{int}$	$L_{int} > 0.66L_{maj}$	Cu-rich tenorite Co-rich spinel
Needle	$L_{min} > 0.66L_{int}$	$L_{int} < 0.66L_{maj}$	Cu-rich tenorite
Plate	$L_{min} < 0.66L_{int}$	$L_{int} < 0.66L_{maj}$	Cu-rich tenorite
Disc	$L_{min} < 0.66L_{int}$	$L_{int} > 0.66L_{maj}$	Not observed
Multi-sphere	$L_{min} > 0.66L_{int}$	$L_{int} < 0.66L_{maj}$	Co-rich spinel

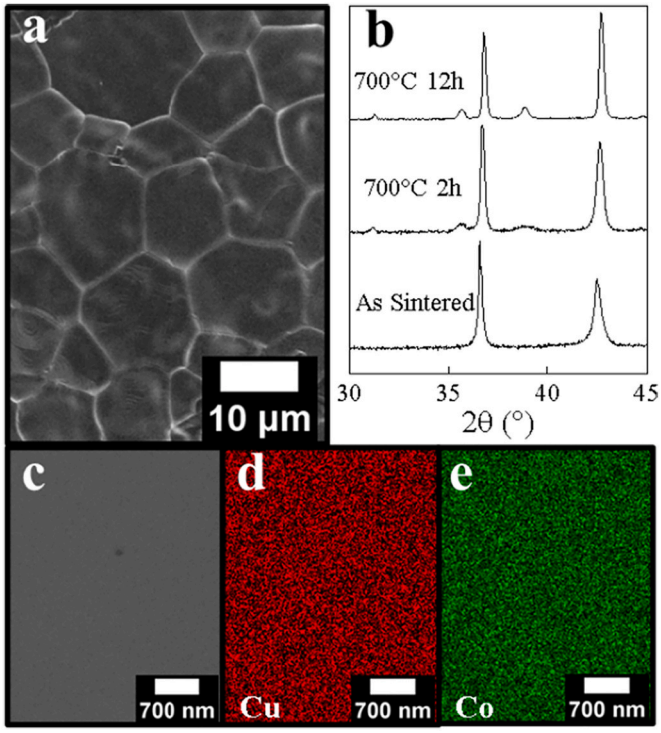

Fig. 4. Microstructure and phase state of the bulk TM-ESO samples. (a): Fracture surface micrographs of the as-sintered sample, (b) XRD patterns of the as-sintered and heat-treated samples (heat treatment conditions are specified), (c) SEM micrograph of the as-sintered sample and the corresponding EDS elemental maps for (d) Cu and (e) Co.

heat treated within the phase transformation temperature window in order to generate a meaningful amount of secondary phase for further study (Fig. 4b). Heat treating the consolidated sample at 700 °C for 2 h yields two sets of secondary phase peaks, with one set of peaks corresponding to the familiar Cu-rich tenorite phase [11]. The additional set of peaks correspond to a Co-rich spinel phase of the form MCo_2O_4 (where M = Cu, Mg, Ni, Zn). Further details on this Co-rich spinel secondary phase are discussed below. The amount of secondary phase was calculated through Rietveld refinement and found to be 7 at.% Cu-rich tenorite and 5 at.% Co-rich spinel. Increasing the heat treatment time to 12 h increases the amount of secondary phase to 15 at.% Cu-rich tenorite and 8 at.% Co-rich spinel. SEM and EDS were used to qualitatively verify the presence of the secondary phases, as seen in Fig. 2b-d. Light and dark regions, corresponding to the nanostructured secondary phase particles, can be observed on the surface of the cuboid and on the individual slices (Fig. 2b). The dark regions possess sphere and needle shaped morphologies, while the light regions are only sphere shaped. EDS analysis of the light and dark regions confirms that they correspond to the Cu-rich tenorite (dark regions) and Co-rich spinel (light region) secondary phases (Fig. 2c and d).

3.2. Tomography of the 2 h heat treated sample

Using FIB tomography, it is possible to observe the 3D features of the secondary phases in TM-ESO with nanoscale resolution. The resulting reconstructed cuboid of the Cu-rich tenorite secondary phase particles (hereafter referred to simply as 'Cu-rich particles') for the sample heat treated for 2 h can be seen in Fig. 1. A significant quantity of Cu-rich particles can be observed in the reconstructed volume. It should be noted, however, that the perceived ubiquity of the Cu-rich particles in Fig. 1 is an artifact of using a two-dimensional figure to visualize a three-dimensional microstructure. The reconstruction consists of 390 Cu-rich particles. Based on the Zingg and Tucker dimensional criteria for defining morphologies (summarized in Table 1), three different morphologies are observed in the cuboid: sphere-like, needle-like, and plate-like morphologies with their various dimensions summarized in Table 2. Particles with disc-like morphologies are not commonly observed in the reconstruction and are therefore not discussed in this work. The size distribution of the dimensions of the Cu-rich particles can be seen in Fig. 5a, with the y-axis being with respect to the volume of the secondary phase itself and not the entire volume of the reconstructed cuboid. The shaded regions in Fig. 5 highlight the distribution of the L_{maj} dimension of the three particle morphologies. Cu-rich particles that have a sphere-like morphology are primarily spherical or oblong in shape, while needle-like particles have a major diameter that is much longer than the intermediate or minor diameter. However, the needle-like particles are not always linear or "straight" in shape, often having some amount of curvature.

Although numerically less common than the sphere-like and needle-like Cu-rich particles, complex plate-like Cu-rich particles with nanostructured dimensions can also be observed in the reconstructed bulk TM-ESO cuboid. Plate-like particles have a major diameter that is longer than the intermediate diameter, and an intermediate diameter that is longer than the minor diameter, giving them an exaggerated "flattened" shape. Additionally, the plate-like particles can form branches and offshoots. Despite the wide range of L_{maj} values observed in the Cu-rich particles (30–570 nm), the L_{min} values of all the measured particles are <100 nm. A nanostructured dimension is observed in all Cu-rich particle morphologies (sphere-, needle-, and plate-like morphologies) and across all particle sizes. Therefore, the majority of the Cu-rich particles are nanostructured along their minor diameter, indicating that the particle growth is significantly anisotropic. It is important to note that the Co-rich spinel phase is not visible after heat treating at 700 °C for 2 h using SEM or EDS, despite being detected using XRD. We hypothesize that the Co-rich particles formed under these heat treatment conditions are too small to be detected during our FIB tomography process. Particles with a dimension smaller than 24 nm were excluded from analysis in this work, indicating that the sphere-like Co-rich particles will have diameters <24 nm after heat treating at 700 °C for 2 h.

A grain boundary intersects part of the cuboid observed in the 2 h sample, which is located in the bottom right corner of the blue outlined region in Fig. 1. The reconstructed cuboid of the Cu-rich particles reveals that the grain boundary consists of Cu-rich particles with sphere-like morphologies. However, these grain boundary particles are noticeably larger than the sphere-like particles found throughout the rest of the

Table 2
Summary of the distribution of the major (L_{maj}), intermediate (L_{int}), and minor (L_{min}) dimensions of the Cu-rich tenorite and Co-rich spinel secondary phase particles after heat treating bulk TM-ESO samples at 700 °C for 2 and 12 h, respectively. The "total" row corresponds to the distributions for all of the particles of that phase, regardless of morphology. Breakdowns for the individual morphologies are also provided.

	L_{min} (nm)	L_{int} (nm)	L_{maj} (nm)
2 h: Cu-rich tenorite secondary phase particles			
Total	30–90	30–200	30–570
Sphere	30–80	30–110	30–160
Needle	30–90	30–110	120–440
Plate	40–90	80–200	260–570
12 h: Cu-rich tenorite secondary phase particles			
Total	30–100	50–320	30–890
Sphere	30–70	50–90	30–160
Needle	30–100	60–150	150–400
Plate	50–100	80–320	310–890
12 h: Co-rich spinel secondary phase particles			
Total	30–150	30–260	40–440
Sphere	30–130	30–260	40–310
Multi-sphere	50–150	60–150	200–440

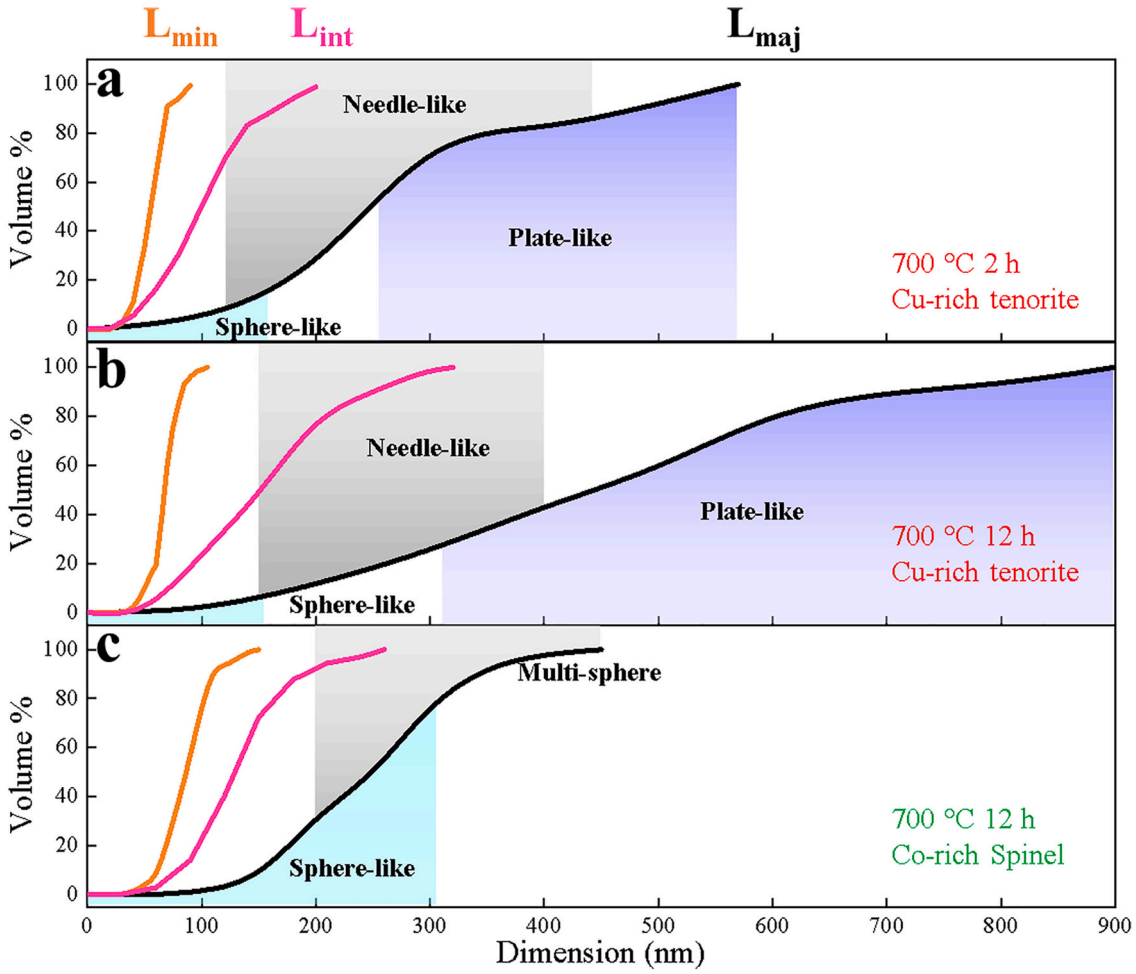

Fig. 5. Role of heat treatment conditions on secondary phase size and morphology in bulk TM-ESO. The size distribution of the dimensions of the Cu-rich tenorite secondary phase particles in the bulk sample heat treated at: a) 700 °C for 2 h, and b) 700 °C for 12 h. c) The size distribution of the dimensions of the Co-rich spinel secondary phase particles in the 12 h sample. The orange curves correspond to the minor diameter (L_{min}) of the particles, demonstrating that most of the secondary phase particles have at least one nanostructured dimension. The pink curves correspond to the intermediate diameter (L_{int}). The black curves correspond to the major diameter (L_{maj}), with the shaded regions of the curve corresponding to the range of L_{maj} values observed for the labeled morphologies. Note that the calculated vol% is with respect to the volume occupied by the respective secondary phase, and not the total volume of the reconstruction. (For interpretation of the references to color in this figure legend, the reader is referred to the web version of this article).

reconstructed cuboid, having L_{maj} values ranging from 160 to 270 nm. Our previous work showed that the Cu-rich tenorite secondary phase is ubiquitous in the grain boundaries throughout the heat treated coarse-grained samples [11]. Additionally, increasing grain boundary content (decreasing grain size) increased the amount of secondary phase that forms. The secondary phases will form more readily on the grain boundaries due to their increased free energy compared to the bulk [31]. We anticipate that the secondary phases form on the grain boundaries first, explaining why the Cu-rich sphere-like particles at the grain boundary are larger than what is found in the rest of the analyzed cuboid.

3.3. Tomography of the 12 h heat treated sample

Our XRD results show that increasing the heat treatment time from 2 h to 12 h at 700 °C results in an increase in the amount of secondary phase that forms. The 3D reconstructed cuboid of the Cu-rich tenorite secondary phase particles for the sample heat treated for 12 h consists of 350 particles and can be observed in Fig. 6. Much like the 2 h sample, sphere-like, needle-like, and plate-like Cu-rich particles are observed in the 12 h sample, with their respective dimensions summarized in Table 2. Similar to the 2 h sample, disc-like morphologies are not commonly observed in the 12 h sample. The size distribution of the dimensions of the Cu-rich particles can be seen in Fig. 5b. Larger particles constitute a greater portion of the total Cu-rich tenorite secondary phase volume compared to the 2 h sample, indicating that increased heat treatment time has caused the secondary phase particles to grow. Sphere-like and needle-like Cu-rich particles in the 12 h sample exhibit similar dimensions to those found in the 2 h sample, indicating that heat treatment time had little effect on the dimensions of Cu-rich particles with these morphologies.

The most significant changes in the Cu-rich particles due to increased heat treatment time from 2 h to 12 h occurs in the plate-like particles. Both the intermediate and major diameters of the plate-like particles have grown as a result of the increased heat treatment time, with L_{maj} values increasing from 260-570 to 310–890 nm. A small number of very large and complex plate-like Cu-rich particles can also be observed in the analyzed cuboid. These particles typically have a major diameter much longer than the intermediate and minor diameter, with L_{maj} values between 500 and 800 nm. Additionally, the plate-like particles have highly complex shapes, often with significant branches and offshoots. Despite their complexity, these Cu-rich particles are still distinctly plate-like, having a minor diameter that is significantly smaller than the intermediate and major diameter.

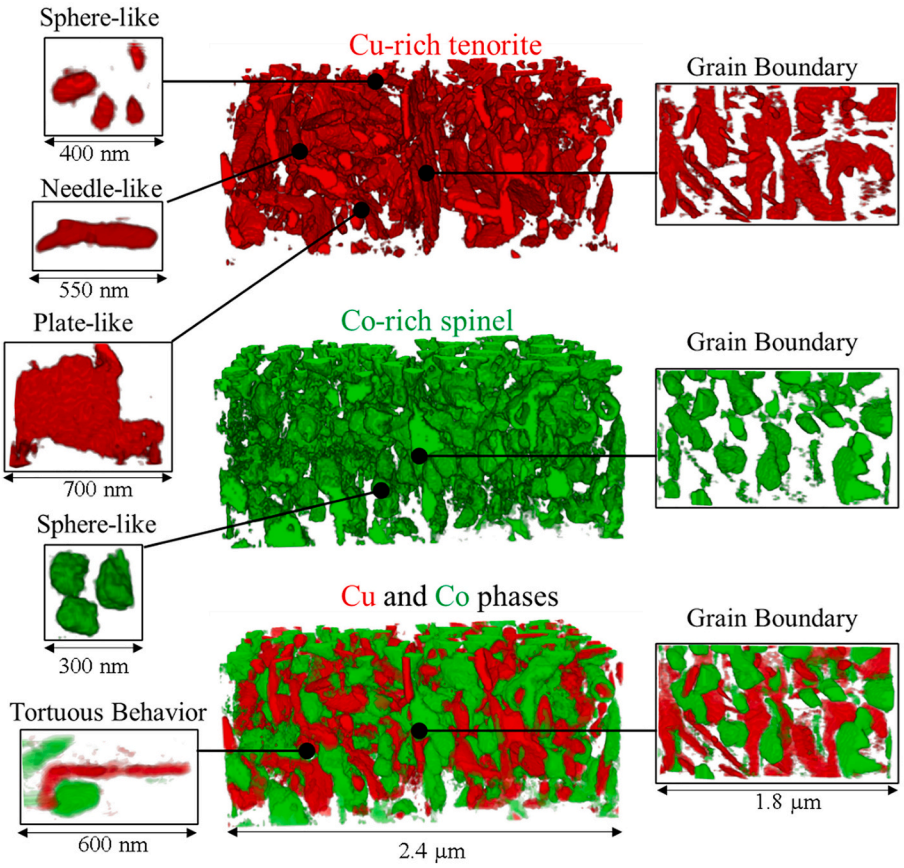

Fig. 6. Morphology and interactions of the secondary phase particles in bulk heat-treated TM-ESO. Reconstructed 3D cuboids from the bulk TM-ESO sample heat treated at 700 °C for 12 h displaying the: a) Cu-rich tenorite secondary phase particles, b) Co-rich spinel secondary phase particles, and c) a composite reconstruction of both the Cu-rich and Co-rich secondary phase particles. Displayed around the reconstructed cuboid are images of individual secondary phase particles that represent specific morphologies or regions of interest.

A grain boundary can be seen bisecting the middle of the observed cuboid in the sample heat treated for 12 h (Fig. 6). Unlike the sphere-like Cu-rich particles at the grain boundary in the 2 h sample, the Cu-rich tenorite secondary phase emerges as a complex plate-like network along the grain boundary of the 12 h sample. A single Cu-rich plate-like network dominates the region of the grain boundary. However, smaller plate-like and needle-like Cu-rich particles can also be observed in the grain boundary as well. The exact dimensions of the particles in the grain boundary are difficult to ascertain due to these particles extending outside the analyzed cuboid. Interestingly, the Cu-rich particles in the grain boundary are oriented the same way, with the major and intermediate diameters being parallel to the grain boundary. Such an observation can be expected when considering the anisotropic growth of the Cu-rich particles and the enhanced diffusion kinetics provided by the grain boundaries. Increasing heat treatment time from 2 h to 12 h allows the Cu-rich particles to grow from simple sphere-like morphologies to large complex plate-like morphologies. Note that there is an approximately 150–200 nm separation between the Cu-rich particles in the grain boundary and the nearest Cu-rich particles in the grain interior. Additionally, no Cu-rich particles intersect or cross the grain boundary from one side to another. Instead, a region free of Cu-rich particles forms around the grain boundary, which we hypothesize is due to the high concentration of Cu-rich tenorite phase in the grain boundary. The Cu-rich grain boundaries deplete the surrounding area of Cu and make it difficult for Cu-rich phase to grow in this “depletion region”.

Perhaps most interesting about the Cu-rich particles in the 12 h sample is the nanostructured thickness dimension (L_{min}) of the observed particles. Much like in the 2 h sample, the L_{min} dimension for all of the Cu-rich particles is predominantly <100 nm. Increased heat treatment time does not significantly influence L_{min} of the Cu-rich particles, only the L_{maj} and L_{int} dimensions of the particles. Our results indicate that the Cu-rich particles will retain their nanostructured thickness regardless of the heat treatment conditions, allowing for the creation of reversible microstructures with nanostructured dimensions.

The Co-rich spinel secondary phase is visible in the 12 h sample, indicating that extended heat treatment times allow the Co-rich spinel particles to grow large enough to be easily observed. A 3D reconstruction of the Co-rich spinel phase can be observed in Fig. 6, and a summary of dimensions for the Co-rich spinel secondary particles (hereafter referred to simply as ‘Co-rich particles’) can be seen in Table 2. The reconstruction consists of 350 Co-rich particles. The size distribution of the dimensions of the Co-rich particles in this sample can be seen in Fig. 5c. Unlike the Cu-rich particles, the Co-rich particles primarily manifest with a sphere-like morphology. These sphere-like particles are commonly oblong in shape. However, many elongated Co-rich particles exist that have a “needle-like” appearance. Closer inspection of these “needle-like” particles reveals that they are two or more sphere-like particles that have “merged” together. We refer to these merged particles as “multi-sphere” particles. The measured L_{min} dimensions of the Co-rich particles are all ≤150 nm. Much like the Cu-rich particles, the majority of the Co-rich particles have a nanostructured dimension, with 75 vol% of the Co-rich particles having a L_{min} value of ≤100 nm.

Unlike the Cu-rich tenorite secondary phase, the Co-rich spinel secondary phase is not significantly represented within the grain boundary in the 12 h sample. We hypothesize that, during heat treatment, the Cu-rich tenorite secondary phase emerges before the Co-rich spinel secondary phase and rapidly populates the grain boundary region, leaving little room for the Co-rich phase to emerge. However, some small amount of Co-rich phase does lie on the grain boundary. It is unlikely that the Co-rich phase nucleates from the grain boundary as the Co-rich particles that contact the grain boundary do not appear on both sides of the boundary, i.e., none of the Co-rich particles are observed intersecting the grain boundary. Instead, a few Co-rich particles appear to grow from the grain interior into the boundary, having their growth halted by the

grain boundary core, unable to cross into the next grain. Additionally, Co-rich particles are able to occupy the region adjacent to the grain boundary, indicating that there is no equivalent depletion region as seen for the Cu-rich phase.

In both the 2 h and 12 h samples, the Cu-rich needle-like and plate-like particles will often exhibit a small amount of curvature. However, some of the Cu-rich particles in the 12 h sample exhibit highly complex curvatures, with ~90° or ~ 180° bends and other tortuous features being observed. Overlaying the Cu-rich and Co-rich secondary phase reconstructions (Fig. 6) reveals that this tortuous behavior often occurs when a Co-rich particle is located near the intermediate or major diameter of a Cu-rich particle, indicating that interactions between the two phases can influence their growth and morphology. Interesting interactions between secondary phases have been observed in other materials, such as in Al—Cu alloys where CuAl precipitates consume or inhibit the growth of other CuAl precipitates [32]. Interactions between distinct insoluble secondary phases have been observed in high entropy alloys such as AlCrCuFeNiZn [33] and $Al_{0.3}CuFeCrNi_2$ [34], where Cu-rich and Cr-rich secondary phases emerge concurrently and influence each other's morphology. The appearance of separate distinct Cu- and Cr-rich phases is attributed to the poor solubility between Cu and Cr [35], which will cause the phases to grow near each other and interact without dissolving into one another. A similar explanation can be given for the heat-treated TM-ESO in this study since the solubility limit of CoO in CuO is <5 at.% for temperatures below 870 °C [36], with CuO and CoO instead forming a two-phase mixture consisting of tenorite CuO and spinel Co_3O_4 [37].We observe no signs of any mixing or reaction between the Cu-rich and Co-rich secondary phases in the heat-treated TM-ESO, indicating that they are insoluble in each other under these conditions. We propose that the Cu-rich particles will grow in such a way as to "avoid" nearby Co-rich particles, resulting in the tortuous behavior that we observe. Interestingly, we observe no obvious analogous behavior in the Co-rich particles.

Our tomography results reveal that the morphology of the Cu-rich and Co-rich secondary phases in TM-ESO are more complex than previously thought [11]. Our previous analysis of the secondary phases was based on SEM and EDS imaging of flat sample surfaces, and was, therefore, unable to discern the true complexity of the secondary phase particles revealed by a 3D perspective. It is, therefore, worth re-evaluating the secondary phase particles using 2D microscopy analysis. EDS composition maps for the 12 h sample can be seen in Fig. 2b–d. Without our tomography results, these images would lead one to believe that the Cu-rich tenorite secondary phase exhibits only sphere-like and needle-like particles and no plate-like particles, and that the Co-rich spinel secondary phase exhibits only sphere-like particles. We note, however, that a needle-like or plate-like particle is statistically unlikely to have its major diameter parallel to the sample surface, as shown schematically in Fig. 7a. Instead, many of the Cu-rich sphere-like particles observed in the 2D SEM and EDS analysis will actually be needle-like particles, the major diameter of which is not parallel to the sample surface (Fig. 7b). Similarly, 2D needle-like particles can actually be plate-like particles, the intermediate or major diameter of which is not parallel to the sample surface. A similar explanation can be given for why the Co-rich multi-sphere particles are not commonly observed in the 2D SEM/EDS analysis.

3.4. Sphericity of the secondary phase particles

Sphericity, which indicates how much the morphology of the particle resembles a sphere, can be used to quantify the morphology of the secondary phase particles. The distribution of the sphericity for the Cu-rich particles in the 2 h heat-treated TM-ESO sample and the Cu- and Co-rich particles in the 12 h heat-treated TM-ESO sample as a function of particle size can be seen in Fig. 8a. The majority of the Cu-rich particles are highly non-spherical, with 90% of the secondary phase volume having sphericities $\Psi < 0.8$. Additionally, increasing the heat-treatment time from 2 to 12 h at 700 °C leads to a greater content of low sphericity particles, with particles having sphericities $\Psi < 0.5$ increasing from 10% to 32% of the total Cu-rich phase volume. Interestingly, the cumulative vol% curves for the Cu-rich particles at the two heat-treatment times converge at sphericities $\Psi \geq 0.8$, indicating that heat-treatment time does not influence the fraction of spherical particles. The interplay between particle size and morphology in the Cu-rich particles is discussed below. In contrast to the Cu-rich particles, the Co-rich particles are overall more spherical, with 73% of the particle volume exhibiting sphericities $\Psi < 0.8$. Additionally, Co-rich particles with sphericities $\Psi \leq 0.5$ are not observed in our tomography results.

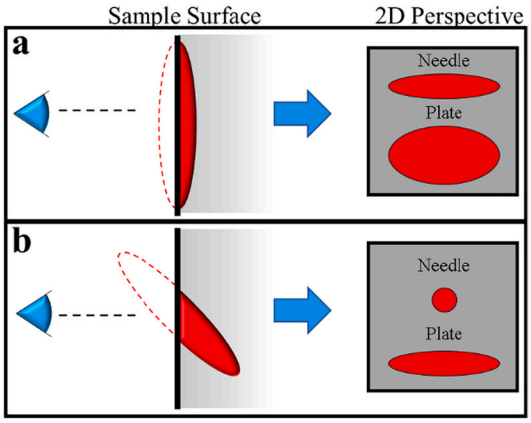

Fig. 7. Misinterpretation of secondary phase particle morphologies when projecting from a 2D image. Schematics showing how the 3D morphology of a needle- or plate-like secondary phase particle will appear in a 2D image (such as a micrograph of a flat surface) when its major and intermediate diameters are: a) parallel to the sample surface, or b) not parallel to the sample surface. The red needle shapes represent needle-like and plate-like particles, with the filled regions corresponding to the region of the particle that exists under the sample surface. The dashed red lines represent an extrapolation of the secondary phase particle morphology out of the sample surface and are included for clarity. Note that scenario (a) is unlikely to occur, indicating that scenario (b) is the most probable interpretation. (For interpretation of the references to color in this figure legend, the reader is referred to the web version of this article).

The relationship between individual particle size and sphericity for the Cu-rich tenorite secondary phase can be more directly visualized in Fig. 8b (note the log scale on the x-axis). A logarithmic relationship between sphericity and Cu-rich particle size can be observed (appearing linear on the semi-log plot), demonstrating that these particles become less spherical as they grow larger. This logarithmic relationship occurs in both the sample heat treated for 2 h and the sample heat treated for 12 h. The sample heat treated for 12 h has a greater number of very large low sphericity Cu-rich particles compared to the 2 h heat treated sample. Increased heat treatment time causes these particles to grow anisotropically, resulting in particles with increased particle sizes and reduced sphericities. It would therefore be expected that the increasing heat treatment times would result in overall fewer smaller Cu-rich particles, as the smaller particles would grow from the heat treatment. However, a significant number of small spherical Cu-rich particles can be found in the analyzed cuboids, regardless of the heat treatment time. The presence of small Cu-rich particles in both samples indicates that new particles are continuously forming during heat treatment.

Although Fig. 8b shows the general decline of sphericity with increasing particle size, it does not specifically describe how the changing particle dimensions contribute to the changing morphology. A Zingg and Tucker scheme, as noted above, was used to categorize individual particles based on their dimensions. Elongation vs flatness for the Cu-rich particles in the 2 h and 12 h samples can be seen in Fig. 9a and b, respectively (note the log scale on the particle size color map). A distinct evolution in relative shape with particle size can be observed in

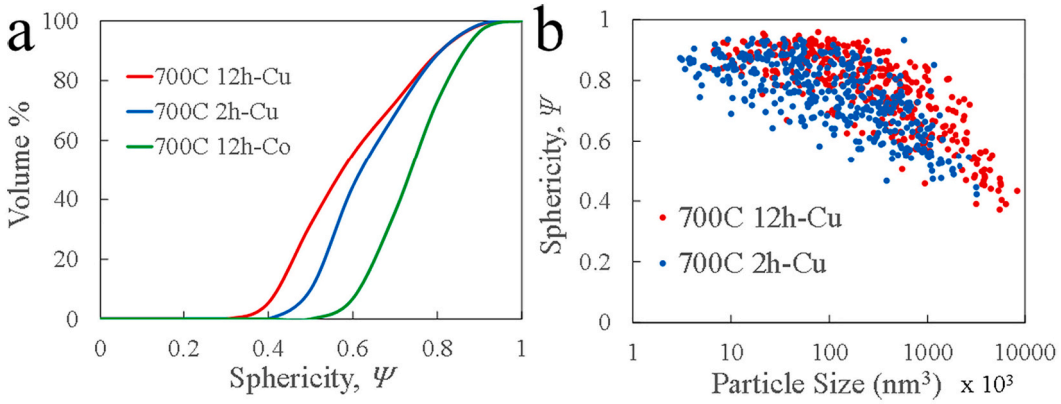

Fig. 8. Influence of secondary phase particle size on sphericity in bulk heat-treated TM-ESO. a) Size distribution of sphericity for the Cu-rich tenorite and Co-rich spinel secondary phase particles in samples heat treated at 700 °C for 2 h and 12 h. b) Sphericity vs particle size for the Cu-rich secondary phase particles in samples heat treated at 700 °C for 2 h and 12 h, illustrating the decline in sphericity with increasing particle size. Note that the calculated vol% is with respect to the volume occupied by the respective secondary phase particles, and not the total volume of the reconstruction.

both samples. Smaller Cu-rich particles ($V = \sim10^4$ nm^3) tend to have high flatness values and elongation values near 0.66, resulting in sphere-like morphologies. As the particles grow ($V = \sim10^5$ nm^3) their elongations decrease (<0.66), yielding particles with a needle-like morphology. Further particle growth ($V = \sim10^6$ nm^3) results in a decrease in the flatness values (<0.66) causing their morphologies to become increasingly plate-like. The morphology evolution of Cu-rich particles is less obvious in the 2 h sample (Fig. 9a), displaying a significant amount of variability in the particle dimensions and morphologies. Conversely, the sphere ➔ needle ➔ plate evolution with particle size is more obvious for the Cu-rich particles in the 12 h sample (Fig. 9b). The increased hold time at 700 °C results in a microstructure that is closer to equilibrium, with fewer outlier morphologies and a very clear particle morphology evolution.

The Zingg and Tucker analysis for the Co-rich particles (Fig. 9c) shows the morphologies for these particles are consistent with our visual observations described in Section 3.3. The sphere-like Co-rich particles have oblong or elongated geometries, which are represented by the significant clustering of particle dimensions near the origin of the four quadrant Zingg and Tucker scheme. The multi-sphere Co-rich particles primarily represent particles with elongations <0.66, which can be classified as "needle-like" morphologies. Unlike the Cu-rich particles, no significant size dependent morphological evolution can be observed in the Co-rich particles.

3.5. Morphological evolution

In many materials, the morphology of secondary phase particles is often determined by the structural and energetic relationship between the primary phase and the secondary phase that forms from it. Isolated precipitates and secondary phase particles are influenced by both interfacial energy and strain that arises from the misfit between the secondary phase and the primary phase [31]. The equilibrium morphology of such particles is dictated by the relative contribution of these two effects. Interfacial energy dominates at small particle sizes, with the equilibrium morphologies being determined by how anisotropic the interfacial energies are. Particles having isotropic surface energies will manifest a spherical shape, while anisotropic surface energies will yield non-spherical particles [31]. Strain energy typically dominates at larger particle sizes when there is misfit strain between the particle and its primary phase, often resulting in anisotropic secondary phase morphologies as a way to minimize the strain energy [38]. Given the increasing importance of elastic strain energy in larger particles, it would be expected that as particles grow there will eventually be a morphological transition. Particles with a meaningful amount of misfit between their primary phase will therefore transition from morphologies determined by interfacial energies to ones determined by strain as the particles grow in size. Such morphological transitions have been observed in various materials, such as the γ-γ' Ni alloy, where γ' precipitates transition from spheres to plates as they grow larger [39].

The growth of secondary phases and precipitates involves the migration of the interface between the new phase and the primary phase. Such migration is often characterized by the mechanism that most limits its motion: diffusion controlled or interface controlled [31]. Incoherent interfaces are known to be diffusion controlled, while coherent and semi-coherent particles are interface controlled [31]. An often-cited feature of high entropy materials is their so called "sluggish diffusion" behavior, which refers to the idea that diffusion is slower in high entropy materials, compared to materials with a single principle element or compound, due to the distribution of atomic radii and bond configurations [40]. Although the sluggish diffusion concept has been called into question in high entropy alloys [41], further work is needed to validate its existence in ESO materials. However, recent work on the transport behavior of TM-ESO demonstrates that this material does not experience sluggish diffusion, instead having a diffusion coefficient that is similar to other oxide ceramics [42]. The absence of sluggish diffusion behavior in TM-ESO suggests that the growth behavior of the secondary phases can be explained through conventional mechanisms.

The morphology of a secondary phase particle is heavily influenced by the nature of the interface between the particle and the primary phase: with secondary phase particles typically being coherent, semi-coherent, or incoherent with the primary phase depending on the level of crystallographic matching that exists between the particle and the primary phase [31]. Coherent and semi-coherent particles can minimize their strain energy by growing along soft crystallographic directions or by growing along lattice planes that minimize misfit between the primary phase and the particle. However, work by Pitike et al. show through experiments and first principles calculations that TM-ESO is mechanically isotropic, i.e., different crystallographic directions in TM-ESO will have similar elastic behavior [43]. Further, simulations by Bhaskar et al. indicate that local cationic stress in multi-phase TM-ESO are unaffected by the orientation between the primary rocksalt phase and the Cu-rich tenorite secondary phase [44]. The above two studies, while still preliminary, indicate that TM-ESO lacks soft crystallographic directions or lattice planes that minimize misfit stress. Therefore, the morphological evolution and anisotropic growth of the Cu-rich particles observed in the present study cannot be entirely attributed to the presence of soft crystallographic directions in the primary rocksalt phase that can reduce the strain energy.

Based on our Zingg and Tucker analysis (Fig. 9), the morphology of

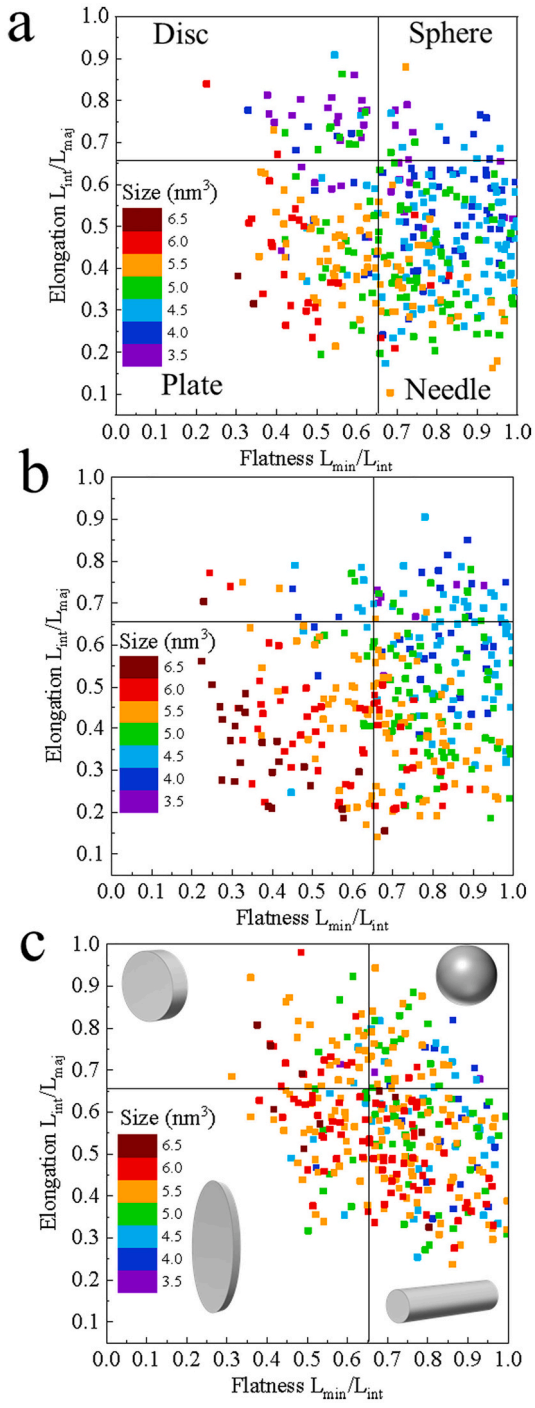

Fig. 9. Particle geometries and morphological classification in bulk heat-treated TM-ESO: Zingg and Tucker schemes plotting the calculated particle elongation vs flatness parameters for: a) the Cu-rich tenorite secondary phase particles in the bulk sample heat treated at 700 °C for 2 h, and b) the Cu-rich tenorite and c) Co-rich spinel secondary phase particles in the bulk sample heat treated at 700 °C for 12 h. The color-coded data points correspond to individual secondary phase particles, with the color indicating the measured size of the particle. The figures are divided into four quadrants for the purpose of classifying the secondary phase particles into one of four geometries (disc, sphere, plate and needle), with schematic examples of the four geometries being displayed in (c).

the Cu-rich particles in heat-treated TM-ESO changes from sphere-like to needle-like to plate-like as the particles grow. The smallest Cu-rich particles exhibit high sphericities ($V \leq 10^4$ nm^3 and $\Psi \geq 0.8$) due to the influence of interfacial energy at these small sizes. It should be noted however that the Cu-rich particles are slightly elongated at this size, indicating that the equilibrium morphology dictated by the interfacial energies is non-spherical. Noting that the Cu-rich particles exhibit the monoclinic (tenorite) structure, it is relevant to also note that simulations of isolated monoclinic particles (independent of a primary phase) are known to form non-spherical morphologies due to their anisotropic interfacial energies [45]. However, the nature of the interaction between the particle and primary phase will modify the particle surfaces and likely lead to deviations from the behavior of an isolated particle. Further work needs to be done to analyze the smaller particles to determine what the equilibrium morphology is with minimal influence from strain energy.

Based on our XRD and Rietveld analysis, the Cu-rich secondary phase has a monoclinic tenorite crystal structure with calculated lattice parameters of a = 4.69 Å, b = 3.41 Å, and c = 5.14 Å, while the primary rocksalt phase has a cubic rocksalt structure with a calculated lattice parameter of a = 4.23 Å. In light of their significant difference in crystal structure, we propose that some or all of the interfaces between an individual Cu-rich particle and the primary rocksalt phase are incoherent when the Cu-rich particle is large. The lack of lattice matching in incoherent interfaces allows them to more easily accommodate atoms being transported across the interfaces, making interface migration in the Cu-rich phase diffusion controlled [31]. Incoherent interfaces are typically more mobile than coherent interfaces. Diffusion controlled interfaces will move as fast as diffusion allows in the system [46], facilitating the substantial morphological changes that we observe.

The observed morphological evolution in the Cu-rich particles is depicted schematically in Fig. 10. The smallest particles we observe typically have an elongated sphere-like appearance. As the Cu-rich particles grow larger, their morphology changes from sphere-like to needle-like and then finally to plate-like. We attribute this evolution in particle morphology to the increasing influence of strain energy as the particle size increases. Strain energy is minimized in incoherent particles by adopting an anisotropic shape, even in an elastically isotropic matrix [47]. The interplay of interfacial and strain energy between the Cu-rich tenorite secondary phase and the primary rocksalt phase yields a system capable of a range of complex particle morphologies. Additionally, no size dependent morphological evolution is observed in the Co-rich particles, indicating minimal misfit strain with the primary rocksalt phase.

It is important to note that the descriptions of the secondary phase particle morphologies and morphological evolution presented in this section are based on visual observations (Figs. 1 and 6) and numerical interpretation (Figs. 8 and 9) of the predominant particle behavior in the analyzed tomographic reconstructions. However, significant scatter in the particle dimensions can be observed in Fig. 9, indicating that many particles defy the trends and observations discussed in this work. We propose two possible explanations for this. First, variability in secondary phase particle morphology could arise from variability in the nucleation conditions of the particles. However, little is currently known about the nucleation behavior of the secondary phases in TM-ESO. Second, the interaction between particles may influence their morphology, leading to the observed variability in particle morphology. As described above, we observe that the presence of the Co-rich particles influence the morphology of the Cu-rich particles, leading to more tortuous morphologies. However, particles of the same composition are also known to influence the morphology of nearby particles. For example, interparticle elastic interactions have been observed to influence secondary phase particle morphology in Ni alloys [39]. More work is needed to better understand the roles that particle interfaces, particle nucleation behavior, and interparticle interactions play in the morphology of the secondary phases in TM-ESO.

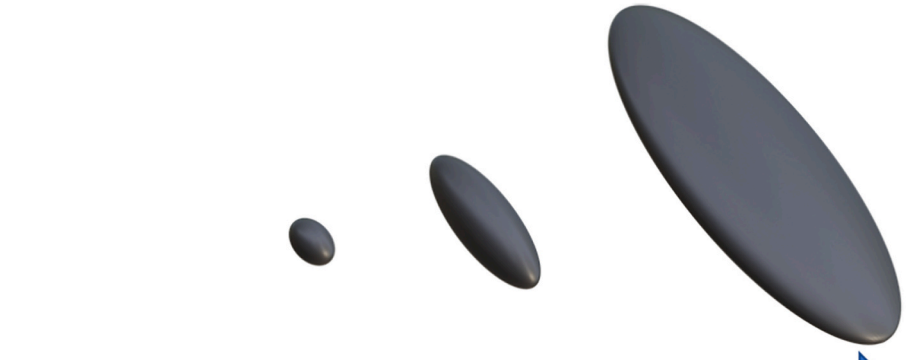

Size (nm³)	10^4	10^5	10^6
Elongation	0.75	0.4	0.4
Flatness	0.85	0.85	0.3

Fig. 10. Size dependent morphological evolution in secondary phase particles: Schematic of idealized particles, illustrating the size dependent morphological evolution in the Cu-rich tenorite secondary phase particles in heat-treated TM-ESO. The three particle morphologies are drawn to scale using the dimensions listed in the table. The dimensions were selected to highlight the sphere→needle→plate particle morphology evolution. Note that the schematic particles have idealized morphologies and are not meant to exactly depict the features of the Cu-rich secondary phase particles.

3.6. Microstructure design

The competition between enthalpy and entropy in ESO materials results in a reversible phase transformation, which leads to a controllable phase heterogeneity (phase spectrum). Our investigation reveals that the morphologies of the Cu-rich and Co-rich particles in TM-ESO can be highly complex, anisotropic, and can have nanostructured dimensions. These features open the door for engineering unique microstructures and nanostructured architectures in ESO materials. In this work, we present two observations with important implications with regard to controlling the secondary phase behavior: 1) the amount of secondary phases, as well as their dimensions and the prevalence of certain morphologies, can be controlled through heat treatment conditions, and 2) different secondary phases can interact with each other in ways that influence their morphology and behavior. We propose that these two principles can be used to control the secondary phase behavior and microstructure of ESO materials in order to engineer bulk samples with specific nanostructured secondary phase architectures and unique properties. These principles, and ideas related to their implementation and consequences, are discussed in more detail below.

Heat treatment conditions: A schematic illustrating how heat treatment time influences the secondary phase content, size, and morphology in TM-ESO is presented in Fig. 11a. In this work we observe that increasing heat treatment time increases the amount and size of the Cu-rich and Co-rich secondary phase particles. The formation of secondary phases in ESO materials is thermodynamically favorable at temperatures below the entropic phase transformation temperature, due to the free energy of the enthalpy-driven phase state outcompeting the free energy of the entropy-driven phase state. In our previous work, we observe that heat treatments within the phase transformation temperature window (650–850 °C) will result in the formation of secondary phases, with heat treatments at 700 °C resulting in the highest amount of secondary phase [11,13]. In this work, we observed that increasing heat treatment time increased the amount of secondary phase that formed. Further, we observed that heat treatment time influences the size distribution, and by extension the morphology, of the secondary phase particles. Given the thermodynamic and kinetic nature of the phase evolution, and the ease of heat treatment, it would be expected that heat treatment conditions will be the major lever in controlling the secondary phase behavior in ESO materials.

Phase-phase interactions: A schematic illustrating how increasing Co-rich phase content influences the behavior of the Cu-rich phase in TM-ESO is presented in Fig. 11b. We observe that the growth of the needle-like and plate-like Cu-rich particles in TM-ESO is modified by the presence of the Co-rich particles, resulting in Cu-rich particles with complex and tortuous morphologies. We propose that the interaction between two phases in an ESO material can be leveraged to engineer the morphology and complexity of one phase by manipulating the other. For example, the Co-rich phase content in TM-ESO could be engineered to control the prevalence of tortuous morphologies in the Cu-rich phase. It would be expected that if we move away from the equiatomic compositions, such as by increasing the amount of CoO in TM-ESO, we could increase the amount of Co-rich secondary phase that can form, leading to an increase in the prevalence of tortuous behavior in the Cu-rich particles. Conversely, decreasing the amount of CoO in TM-ESO should decrease the amount of Co-rich phase, and thus the prevalence of tortuous behavior in the Cu-rich particles.

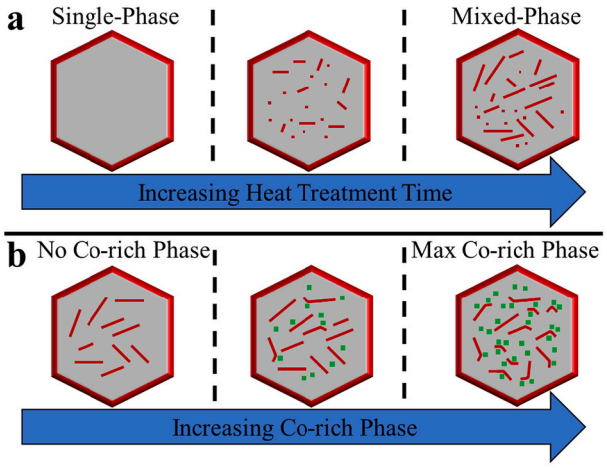

Fig. 11. Strategies for controlling the microstructure and secondary phase morphologies in TM-ESO. Schematics demonstrating two ways that the secondary phase particles can be controlled in ESO materials, and how those methods manifest in TM-ESO. The methods include: a) controlling the amount, size, and morphology of the secondary phase particles using heat treatment conditions, and b) engineering the morphology of one secondary phase by introducing an additional secondary phase.

Taken together, we show that the complex morphology of the secondary phases in ESO materials is controllable using heat treatment conditions and phase-phase interactions. The available complexity of

the secondary phases allows for considerable opportunities for microstructure engineering, nanostructured architectures, and the tuning of properties. An entropic transformation and the resulting phase transformation behavior will be inherent to any material that is truly entropy stabilized. However, the exact manifestation of the entropic transformation will depend on the chemistry and properties of the ESO material. Little attention has been paid to discovering ESO materials with a reversible phase transformation. Instead, the primary trend in the literature is to explore HEO systems that produce single-phase materials. We hypothesize that phase transformation and morphological behavior similar to that observed here for TM-ESO will be found in other HEO materials, providing motivation to reassess previously studied HEO systems as well as the strategies for future HEO development. Further, entropic stabilization is a compositional materials design strategy, and can be applied to a wide range of material categories, crystal structures, and applications. Our work demonstrates that the competition between enthalpy and entropy gives ESO materials unparalleled opportunities for microstructural design, and that these phenomena are worth exploring in other ESO materials. Clever materials engineering will allow the entropic phase transformation to be leveraged for designing materials with specific microstructures and complex architectures, creating unique properties and novel functionalities.

4. Conclusions

FIB tomography was used to observe the morphologies of enthalpy-driven secondary phases in bulk TM-ESO samples after heat treatment. The morphology of the Cu-rich tenorite secondary phase is significantly more complex than previously thought, exhibiting sphere-, needle-, and plate-like particles with one or more nanostructured dimension. The morphology of the Cu-rich secondary phase particles changes with particle size, demonstrating a sphere➔needle➔plate-like evolution as the particle size increases. A Co-rich spinel secondary phase was also observed and found to have a sphere-like morphology. Taken together, the size and morphology of these secondary phase particles are influenced by heat treatment conditions and interactions with other secondary phase particles, providing ESO materials with a significant degree of control over the morphology and distribution of the secondary phase particles. Based on these observations, we propose that the entropic phase transformation in ESO materials can be used to design complex microstructures without significantly altering the primary phase or chemistry. The strategies that we have outlined in this paper will make it possible to engineer bulk ESO materials with a variety of nanostructured features, providing a powerful tool for controlling and enhancing properties, functionality and performance. We believe that this behavior exists in other ESO materials as well, including compositions that were disregarded for not exhibiting an entropy-stabilized phase. Our work provides a compelling reason to explore HEO systems that exhibit phase transformations and re-evaluate future HEO design priorities.

Data Availability

The raw/processed data required to reproduce these findings cannot be shared at this time as the data also forms part of an ongoing study.

Declaration of Competing Interest

The authors declare that they have no known competing financial interests or personal relationships that could have appeared to influence the work reported in this paper.

Acknowledgements

The authors acknowledge the use of facilities and instrumentation at the UC Irvine Materials Research Institute (IMRI), which is supported in part by the National Science Foundation through the UC Irvine Materials Research Science and Engineering Center (DMR-2011967). Funding was provided by the UCI Samueli School of Engineering and the National Science Foundation under award CMMI-2029966.

References

[1] C.M. Rost, E. Sachet, T. Borman, A. Moballegh, E.C. Dickey, D. Hou, J.L. Jones, S. Curtarolo, J.-P. Maria, Entropy-stabilized oxides, Nat. Commun. 6 (2015) 8485, https://doi.org/10.1038/ncomms9485.
[2] D. Bérardan, S. Franger, D. Dragoe, A.K. Meena, N. Dragoe, Colossal dielectric constant in high entropy oxides, Phys. Status Solidi - Rapid Res. Lett. 10 (2016) 328–333, https://doi.org/10.1002/pssr.201600043.
[3] A. Sarkar, L. Velasco, D. Wang, Q. Wang, G. Talasila, L. de Biasi, C. Kübel, T. Brezesinski, S.S. Bhattacharya, H. Hahn, B. Breitung, High entropy oxides for reversible energy storage, Nat. Commun. 9 (2018) 3400, https://doi.org/10.1038/s41467-018-05774-5.
[4] D. Bérardan, S. Franger, A.K. Meena, N. Dragoe, Room temperature lithium superionic conductivity in high entropy oxides, J. Mater. Chem. A 4 (2016) 9536–9541, https://doi.org/10.1039/C6TA03249D.
[5] H. Chen, J. Fu, P. Zhang, H. Peng, C.W. Abney, K. Jie, X. Liu, M. Chi, S. Dai, Entropy-stabilized metal oxide solid solutions as CO oxidation catalysts with high-temperature stability, J. Mater. Chem. A 6 (2018) 11129–11133, https://doi.org/10.1039/C8TA01772G.
[6] A. Sarkar, R. Djenadic, D. Wang, C. Hein, R. Kautenburger, O. Clemens, H. Hahn, Rare earth and transition metal based entropy stabilised perovskite type oxides, J. Eur. Ceram. Soc. 38 (2018) 2318–2327, https://doi.org/10.1016/j.jeurceramsoc.2017.12.058.
[7] J. Gild, M. Samiee, J.L. Braun, T. Harrington, H. Vega, P.E. Hopkins, K. Vecchio, J. Luo, High-entropy fluorite oxides, J. Eur. Ceram. Soc. 38 (2018) 3578–3584, https://doi.org/10.1016/j.jeurceramsoc.2018.04.010.
[8] J. Gild, Y. Zhang, T. Harrington, S. Jiang, T. Hu, M.C. Quinn, W.M. Mellor, N. Zhou, K. Vecchio, J. Luo, High-entropy metal diborides: a new class of high-entropy materials and a new type of ultrahigh temperature ceramics, Sci. Rep. 6 (2016) 37946, https://doi.org/10.1038/srep37946.
[9] A.L. Vyatskikh, B.E. MacDonald, A.D. Dupuy, E.J. Lavernia, J.M. Schoenung, H. Hahn, High entropy silicides: CALPHAD-guided prediction and thin film fabrication, Scr. Mater. 201 (2021), 113914, https://doi.org/10.1016/j.scriptamat.2021.113914.
[10] T.J. Harrington, J. Gild, P. Sarker, C. Toher, C.M. Rost, O.F. Dippo, C. McElfresh, K. Kaufmann, E. Marin, L. Borowski, P.E. Hopkins, J. Luo, S. Curtarolo, D. W. Brenner, K.S. Vecchio, Phase stability and mechanical properties of novel high entropy transition metal carbides, Acta Mater. 166 (2019) 271–280, https://doi.org/10.1016/J.ACTAMAT.2018.12.054.
[11] A.D. Dupuy, X. Wang, J.M. Schoenung, Entropic phase transformation in nanocrystalline high entropy oxides, Mater. Res. Lett. 7 (2019) 60–67, https://doi.org/10.1080/21663831.2018.1554605.
[12] A.D. Dupuy, M.R. Chellali, H. Hahn, J.M. Schoenung, Multiscale phase homogeneity in bulk nanocrystalline high entropy oxides, J. Eur. Ceram. Soc. 41 (2021) 4850–4858, https://doi.org/10.1016/j.jeurceramsoc.2021.03.035.
[13] A.D. Dupuy, I.-T. Chiu, P. Shafer, E. Arenholz, Y. Takamura, J.M. Schoenung, Hidden transformations in entropy-stabilized oxides, J. Eur. Ceram. Soc. 41 (2021) 6660–6669, https://doi.org/10.1016/j.jeurceramsoc.2021.06.014.
[14] S.N. Monteiro, S. Paciornik, From historical backgrounds to recent advances in 3D characterization of materials: An overview, JOM. 69 (2017) 84–92, https://doi.org/10.1007/s11837-016-2203-8.
[15] H. Wu, Y. Yao, Y. Zhou, F. Qiu, Analyses of representative elementary volume for coal using X-ray μ-CT and FIB-SEM and its application in permeability predication model, Fuel. 254 (2019), 115563, https://doi.org/10.1016/j.fuel.2019.05.146.
[16] D. Gostovic, N.J. Vito, K.A. O'Hara, K.S. Jones, E.D. Wachsman, Microstructure and connectivity quantification of complex composite solid oxide fuel cell electrode three-dimensional networks, J. Am. Ceram. Soc. 94 (2011) 620–627, https://doi.org/10.1111/j.1551-2916.2010.04111.x.
[17] J.A. Taillon, C. Pellegrinelli, Y.-L. Huang, E.D. Wachsman, L.G. Salamanca-Riba, Improving microstructural quantification in FIB/SEM nanotomography, Ultramicroscopy. 184 (2018) 24–38, https://doi.org/10.1016/j.ultramic.2017.07.017.
[18] J. Zhang, J. Yan, S. Calder, Q. Zheng, M.A. McGuire, D.L. Abernathy, Y. Ren, S. H. Lapidus, K. Page, H. Zheng, J.W. Freeland, J.D. Budai, R.P. Hermann, Long-range antiferromagnetic order in a rocksalt high entropy oxide, Chem. Mater. 31 (2019) 3705–3711, https://doi.org/10.1021/acs.chemmater.9b00624.
[19] K. Chen, X. Pei, L. Tang, H. Cheng, Z. Li, C. Li, X. Zhang, L. An, A five-component entropy-stabilized fluorite oxide, J. Eur. Ceram. Soc. 38 (2018) 4161–4164, https://doi.org/10.1016/j.jeurceramsoc.2018.04.063.
[20] A. Sarkar, Q. Wang, A. Schiele, M.R. Chellali, S.S. Bhattacharya, D. Wang, T. Brezesinski, H. Hahn, L. Velasco, B. Breitung, High-entropy oxides: fundamental aspects and electrochemical properties, Adv. Mater. 31 (2019) 1806236, https://doi.org/10.1002/adma.201806236.
[21] A. Sarkar, R. Djenadic, N.J. Usharani, K.P. Sanghvi, V.S.K. Chakravadhanula, A. S. Gandhi, H. Hahn, S.S. Bhattacharya, Nanocrystalline multicomponent entropy stabilised transition metal oxides, J. Eur. Ceram. Soc. 37 (2017) 747–754, https://doi.org/10.1016/j.jeurceramsoc.2016.09.018.

[22] L. Lutterotti, M. Bortolotti, G. Ischia, I. Lonardelli, H.-R. Wenk, Rietveld texture analysis from diffraction images, Zeitschrift Für Krist. Suppl. 26 (2007) 125–130, https://doi.org/10.1524/zksu.2007.2007.suppl_26.125.
[23] T. Ishitani, H. Kaga, Calculation of local temperature rise in focused-ion-beam sample preparation, J. Electron Microsc. 44 (1995) 331–336, https://doi.org/10.1093/oxfordjournals.jmicro.a051185.
[24] J. Schindelin, I. Arganda-Carreras, E. Frise, V. Kaynig, M. Longair, T. Pietzsch, S. Preibisch, C. Rueden, S. Saalfeld, B. Schmid, J.-Y. Tinevez, D.J. White, V. Hartenstein, K. Eliceiri, P. Tomancak, A. Cardona, Fiji: an open-source platform for biological-image analysis, Nat. Methods 9 (2012) 676–682, https://doi.org/10.1038/nmeth.2019.
[25] B. Münch, Xlib (ImageJ / Fiji plugins), (n.d.). http://wiki.imagej.net/Xlib.
[26] M. Doube, M.M. Kłosowski, I. Arganda-Carreras, F.P. Cordelières, R.P. Dougherty, J.S. Jackson, B. Schmid, J.R. Hutchinson, S.J. Shefelbine, BoneJ: free and extensible bone image analysis in ImageJ, Bone. 47 (2010) 1076–1079, https://doi.org/10.1016/j.bone.2010.08.023.
[27] S. Cao, M. Nishida, D. Schryvers, Quantitative three-dimensional analysis of Ni4Ti3 precipitate morphology and distribution in polycrystalline Ni–Ti, Acta Mater. 59 (2011) 1780–1789, https://doi.org/10.1016/j.actamat.2010.11.044.
[28] D. Tolnai, G. Requena, P. Cloetens, J. Lendvai, H.P. Degischer, Sub-micrometre holotomographic characterisation of the effects of solution heat treatment on an AlMg7.3Si3.5 alloy, Mater. Sci. Eng. A 550 (2012) 214–221, https://doi.org/10.1016/j.msea.2012.04.060.
[29] T. Zingg, Beitrag zur Schotteranalyse. Ph.D. Thesis, ETH Zurich, Zurich, Switzerland, 1935.
[30] M.E. Tucker, Einführung in die Sedimentpetrologie, Ferdinand Enke Verlag, Stuttgart, 1985.
[31] D.A. Porter, K.E. Easterling, M.Y. Sherif, Phase Transformations in Metals and Alloys, Third edition, CRC Press, 2009, https://doi.org/10.1201/9781439883570.
[32] C. Liu, S.K. Malladi, Q. Xu, J. Chen, F.D. Tichelaar, X. Zhuge, H.W. Zandbergen, In-situ STEM imaging of growth and phase change of individual CuAlX precipitates in Al alloy, Sci. Rep. 7 (2017) 2184, https://doi.org/10.1038/s41598-017-02081-9.
[33] K.G. Pradeep, N. Wanderka, P. Choi, J. Banhart, B.S. Murty, D. Raabe, Atomic-scale compositional characterization of a nanocrystalline AlCrCuFeNiZn high-entropy alloy using atom probe tomography, Acta Mater. 61 (2013) 4696–4706, https://doi.org/10.1016/j.actamat.2013.04.059.
[34] B. Gwalani, D. Choudhuri, V. Soni, Y. Ren, M. Styles, J.Y. Hwang, S.J. Nam, H. Ryu, S.H. Hong, R. Banerjee, Cu assisted stabilization and nucleation of L12 precipitates in Al0.3CuFeCrNi2 fcc-based high entropy alloy, Acta Mater. 129 (2017) 170–182, https://doi.org/10.1016/j.actamat.2017.02.053.
[35] S. Curtarolo, G.L.W. Hart, M.B. Nardelli, N. Mingo, S. Sanvito, O. Levy, The high-throughput highway to computational materials design, Nat. Mater. 12 (2013) 191–201, https://doi.org/10.1038/nmat3568.
[36] F.C.M. Driessens, G.D. Rieck, H.N. Coenen, Phase equilibria in the system cobalt oxide/copper oxide in air, J. Inorg. Nucl. Chem. 30 (1968) 747–753, https://doi.org/10.1016/0022-1902(68)80435-X.
[37] L.A. Zabdyr, O.B. Fabrichnaya, Phase equilibria in the cobalt oxide-copper oxide system, J. Phase Equilibria. 23 (2002) 149–155, https://doi.org/10.1361/1054971023604161.
[38] W.C. Johnson, M.B. Berkenpas, D.E. Laughlin, Precipitate shape transitions during coarsening under uniaxial stress, Acta Metall. 36 (1988) 3149–3162, https://doi.org/10.1016/0001-6160(88)90051-X.
[39] A.C. Lund, P.W. Voorhees, The effects of elastic stress on microstructural development: the three-dimensional microstructure of a γ–γ' alloy, Acta Mater. 50 (2002) 2585–2598, https://doi.org/10.1016/S1359-6454(02)00087-3.
[40] K.-Y. Tsai, M.-H. Tsai, J.-W. Yeh, Sluggish diffusion in Co–Cr–Fe–Mn–Ni high-entropy alloys, Acta Mater. 61 (2013) 4887–4897, https://doi.org/10.1016/j.actamat.2013.04.058.
[41] D.B. Miracle, O.N. Senkov, A critical review of high entropy alloys and related concepts, Acta Mater. 122 (2017) 448–511, https://doi.org/10.1016/j.actamat.2016.08.081.
[42] Z. Grzesik, G. Smoła, M. Stygar, J. Dąbrowa, M. Zajusz, K. Mroczka, M. Danielewski, Defect structure and transport properties in (Co,Cu,Mg,Ni,Zn)O high entropy oxide, J. Eur. Ceram. Soc. 39 (2019) 4292–4298, https://doi.org/10.1016/j.jeurceramsoc.2019.06.018.
[43] K.C. Pitike, A.E. Marquez-Rossy, A. Flores-Betancourt, D.X. Chen, K. Santosh, V. R. Cooper, E. Lara-Curzio, On the elastic anisotropy of the entropy-stabilized oxide (Mg, Co, Ni, Cu, Zn)O compound, J. Appl. Phys. 128 (2020), 015101, https://doi.org/10.1063/5.0011352.
[44] L.K. Bhaskar, V. Nallathambi, R. Kumar, Critical role of cationic local stresses on the stabilization of entropy-stabilized transition metal oxides, J. Am. Ceram. Soc. 103 (2020) 3416–3424, https://doi.org/10.1111/jace.17029.
[45] W. Piskorz, J. Gryboś, F. Zasada, S. Cristol, J.-F. Paul, A. Adamski, Z. Sojka, Periodic DFT and atomistic thermodynamic modeling of the surface hydration equilibria and morphology of monoclinic ZrO 2 nanocrystals, J. Phys. Chem. C 115 (2011) 24274–24286, https://doi.org/10.1021/jp2086335.
[46] C.S. Montross, Subeutectoid precipitate growth activation energies in Mg-PSZ, J. Eur. Ceram. Soc. 13 (1994) 395–401, https://doi.org/10.1016/0955-2219(94)90016-7.
[47] J.K. Lee, W.C. Johnson, Re-examination of the elastic strain energy of an incoherent ellipsoidal precipitate, Acta Metall. 26 (1978) 541–545, https://doi.org/10.1016/0001-6160(78)90106-2.